ADVANCED FUNCTIONAL MATERIALS
www.afm-journal.de

Mesostructured Arrays of Nanometer-spaced Gold Nanoparticles for Ultrahigh Number Density of SERS Hot Spots

Ying-Huang Lai, Shiaw-Woei Chen, Michitoshi Hayashi, Ying-Jen Shiu, Chiao-Cheng Huang, Wei-Tsung Chuang, Chun-Jen Su, Hu-Cin Jeng, Jhe-Wei Chang, Yao-Chang Lee, An-Chung Su, Chung-Yuan Mou, and U-Ser Jeng**

A novel one-trough synthesis via an air-water interface is demonstrated to provide hexagonally packed arrays of densely spaced metallic nanoparticles (NPs). In the synthesis, a mesostructured polyoxometalate (POM)-silicatropic template (PSS) is first self-assembled at the air-water interface; upon UV irradiation, anion exchange cycles enable the free-floating PSS film to continuously uptake gold precursors from the solution subphase for diffusion-controlled and POM-site-directed photoreduction inside the silica channels. NPs ≈ 2 nm can hence be homogeneously formed inside the silica-surfactant channels until saturation. As revealed via X-ray diffraction, small-angle X-ray scattering (SAXS), grazing incidence SAXS, and transmission electron microscopy, the Au NPs directed by the PSS template are arrayed into a 2D hexagonal lattice with inter-channel spacing of 3.2 nm and a mean along-channel NP spacing of 2.8 nm. This corresponds to an ultra-high number density (≈10^{19} NPs cm^{-3}) of narrowly spaced Au NPs in the Au-NP@PSS composite, leading to 3D densely deployed hot-spots along and across the mesostructured POM-silica channels for surface-enhanced Raman scattering (SERS). Consequently, the Au-NP@PSS composite exhibits prominent SERS with 4-mercaptobenzoic acid (4-MBA) adsorbed onto Au NPs. The best 4-MBA detection limit is 5 nM, with corresponding SERS enhancement factors above 10^8.

1. Introduction

Intensively studied recently is the application of patterned gold or silver nanoparticles (NP) for surface-enhanced Raman scattering (SERS) towards single molecular sensing.[1] Both experimental[2] and theoretical[3] works have demonstrated drastic SERS effects when the gaps of the 2D-patterned metallic NPs are reduced to ≈1 nm for extreme SERS hot-spot effects. These studies stimulate keen interests in fabricating 3D mesomorphically ordered arrays of closely packed metallic NPs, aiming for an ultrahigh number density of NPs at small gaps ≈1 nm. Previously, 2D-patterned metallic NP arrays were demonstrated from elaborate point-by-point NP printing in a limited zone.[4–6] Alternatively, self-assembly of copolymer-NP composites might indeed facilitate large-area ordering of NPs; however,[7–11] the resulted NP spacing was often significantly larger than a few nanometers whereas the required surface modification

Prof. Y.-H. Lai, S.-W. Chen, C.-C. Huang, H.-C Jeng, J.-W. Chang
Department of Chemistry
Tunghai University
Taichung 407, Taiwan
E-mail: yhlai@go.thu.edu.tw
Dr. M. Hayashi
Center of Condensed Matter Science
National Taiwan University
Taipei 106, Taiwan
Dr. Y.-J. Shiu
Department of Applied Chemistry
National Chiao Tung University
Hsinchu 300, Taiwan
Dr. W.-T. Chuang, Dr. C.-J. Su, Dr. Y.-C. Lee, Prof. U.-S. Jeng
National Synchrotron Radiation Research Center
Hsinchu Science Park
Hsinchu 300, Taiwan
E-mail: usjeng@nsrrc.org.tw
Prof. A.-C. Su
Department of Chemical Engineering
National Tsing Hua University
Hsinchu 300, Taiwan
Prof. C.-Y. Mou
Department of Chemistry
National Taiwan University
Center of Condensed Matter Science
National Taiwan University
Taipei 106, Taiwan

DOI: 10.1002/adfm.201303724

(to prevent NP aggregation) substantially hampered the NP surface activity. As a third approach, hard templates based on mesostructured silica[12–17] or metal-organic frameworks[18,19] have been adopted to synthesize arrayed metallic NPs of well-controlled size and high number density. In this type of templating, metallic NPs were either diffused into silicate channels or directly formed inside the pores of silica templates. Nevertheless, metallic NPs hence incorporated into the templates were often frustrated with irregularly distributed or bunched NPs inside the template pores with uncontrollable pore-blocking.[12–17] Although there are abundant reports for formation of mesostructured materials,[12–19] great challenges remain in incorporating metallic NPs into these well-documented mesostructured templates for 3D densely organized metallic NPs of small gaps for SERS hot spots.

In this study, we adopt the hard template approach and demonstrate a novel one-trough synthesis scheme that can provide closely packed, mesostructurally arrayed metallic NPs with 1–2 nm gaps for high SERS performance. Note that preparation of densely and uniformly populated metallic NPs inside mesopores are known to be extremely difficult via the commonly used reduction by hydrogen, NBH_4, or electrodeposition.[20–23] The key hindrance lies in that continuous reduction of metallic ions, especially Au(III), and pore-filling of NPs could not be sustained due to self pore-blocking by tempo-incoherent formation of NPs inside the channel pores (a consequence of kinetically controlled reactions for NP formation). In contrast to all previous attempts using silica-based templates of calcinated pores in bulk solution,[12–17,20–23] we have developed a polyoxometalate (POM)-silicate-surfactant (PSS) template self-assembled at the air-water interface, allowing diffusion-controlled formation of metallic NPs inside photocatalytic silica channels.[23,24] The proposed free-floating PSS template can provide a platform for uniform and continuous uptake of metallic precursors from the solution subphase (metal ion reservoir). With photocatalytic POM embedded along the silicate-surfactant channels, ongoing cycles of adsorption and POM site-directed reduction of the metallic precursors upon UV irradiation result in nearly monodisperse NPs homogeneously arrayed in the mesostructured silica channels for a final product of

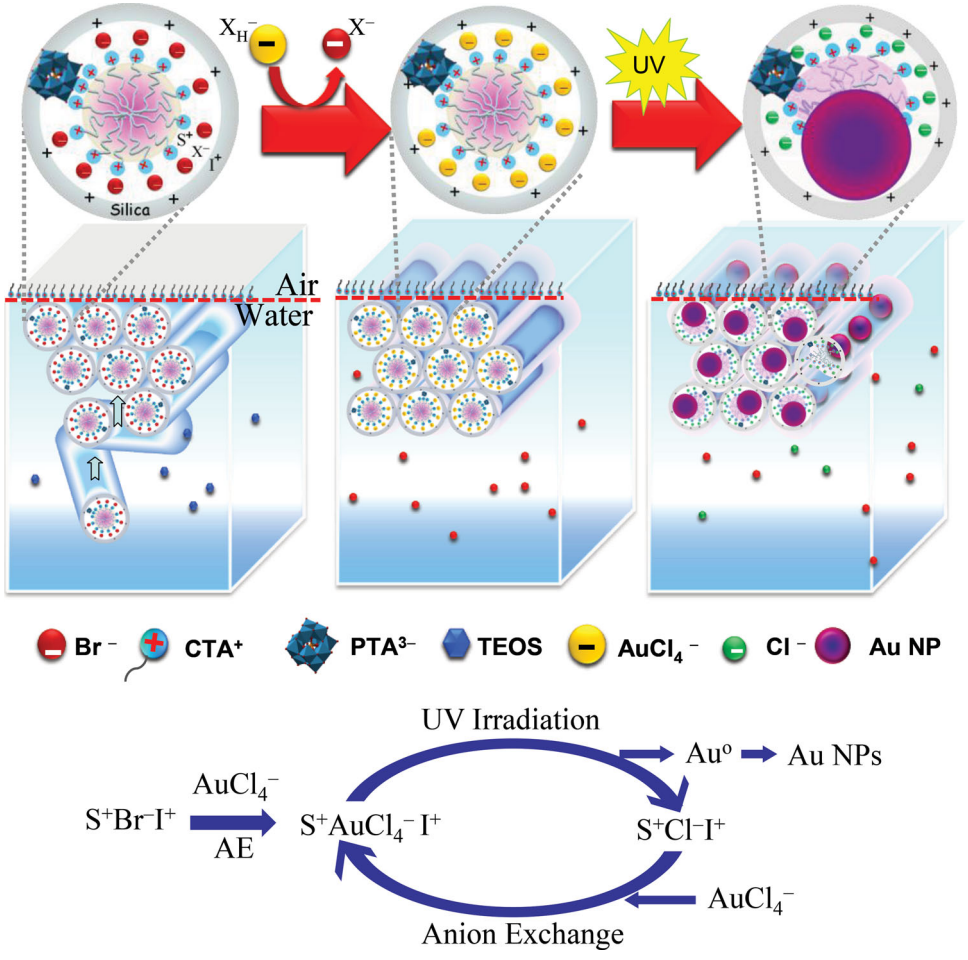

Figure 1. Air-water synthesis scheme for Au-NP@PSS films: from the self-assembled cylinder micelles of POM (PTA^{3-}), silica (I^+; TEOS), and surfactant (S^+X^-; CTAB) phase-separating to the air-water interface for formation of a mesostructured PSS film of 2D hexagonal packing (left), followed by adsorption of metallic precursors (X_H^-; $AuCl_4^-$) into the PSS film via anion exchange (middle), then POM-site-directed reduction and NP formation inside the silicate-surfactant channels upon UV irradiation (right). Given at bottom is a schematic illustration of the anion exchange cycle activated by UV irradiation for a continuous supply of Au atoms for uniform NP formation inside the silica channels.

metallic-NP@PSS composite films. All these processes can be accomplished at the air-water interface of one same trough. Moreover, such metallic-NP@PSS films hence self-assembled at the air-water interface are largely free from contamination of residual reactants in the subphase (i.e., the bulk solution), and are readily transferable to solid substrates or harvested as free-standing films for subsequent uses without need of further purification. Film dimensions can be flexibly controlled by the dimensions of the reaction trough used, i.e., up to centimeters in film lateral dimensions and sub-millimeter in film thickness. The popular evaporation-induced self-assembly (EISA) approach[25,26] would be difficult to adapt this one-trough synthesis protocol, as matured EISA films are confined on solid substrates without the solution subphase (which is subsequently needed for uniform deposition of NPs).

With the proposed synthesis protocol, we have successfully fabricated a new Au-NP@PSS composite, having 3D densely spaced gold NPs of ≈2 nm. We further show that the new composite can exhibit prominent SERS with absorbed 4-mercaptobenzoic acid (4-MBA). As detailed in this report, the high SERS performance can be attributed to the electromagnetic (EM) enhancement from the rich SERS hot spots of the 3D nanometer-spaced Au NPs of ultrahigh number density (≈10^{19} NPs cm^{-3}); strong near-field localized surface plasmon resonance (LSPR) from collective effects of the densely organized small NPs in the Au-NP@PSS composite appears to compensate diminished far-field LSPR from individual NPs.[27] In addition, observed mode-sensitive SERS enhancements reveal an adjunctive chemical effect,[27,28] which is attributable to POM-embedded channel environment according to results of density functional theory (DFT) calculations.[29–32]

2. Results and Discussion

2.1. Synthesis Scheme

Figure 1 illustrates the concept of one-trough synthesis for the PSS and the subsequent metallic NP@PSS films at the air-water interface. In the acidic solution, cationic surfactants, polyoxometalate (e.g., PTA), and silicate source, self-assemble into surfactant-POM-silicate micelles, with $S^+X^-I^+$ counterion bridging where S^+ stands for the surfactant cation (e.g., CTA^+), X^- the anion of the surfactant (or POM), and I^+ the protonated silanols (e.g., TEOS).[33–36] After formation, the relatively hydrophobic POM-silicate-surfactant micelles migrate (phase-separated) from the bulk solution to the air-water interface, and condense into a film of oriented silicatropic mesophase, as that reported previously for similar silica-surfactant systems without POM.[37–40] Further circulation of halide metallic anions (X_H^-) of a higher salting-in strength[41] into the solution beneath this free-standing film enables uniform adsorption of the metallic precursors to the cationic micelle surfaces via anion exchange, i.e., replacing the anion X^- in the $S^+X^-I^+$ coupling by X_H^- for $S^+X_H^-I^+$ coupling, as illustrated in Figure 1.[41] Upon UV irradiation, localized metallic anions can be reduced into atoms for NP formation inside the channels of the POM-silicatropic mesophase via the POM-site-directed photoreduction. Note that the self-sustained anion exchange cycles upon UV irradiation (cf. Figure 1) play a pivotal role in self-sustained pumping metal ions from the subphase reservoir for continuous metal atom reduction and uniform NP formation inside the silica channels of the free-floating film at the air-water interface.

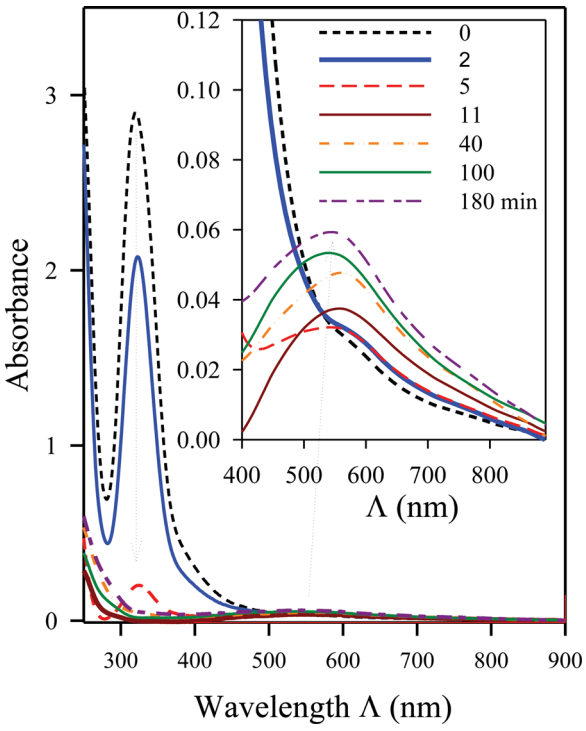

Figure 2. Time-resolved UV-Vis spectra measured for a film of $HAuCl_4$@PSS during UV irradiation. The arrows indicate the quickly decayed 320 nm band owing to reduction of Au^{3+} and slowly enhanced 530 nm band (inset) due to NP formation.

Figure 2 shows the time-dependent UV-vis spectra measured for an $AuCl_4^-$-adsorbed PSS template film during UV irradiation. Adsorption of $AuCl_4^-$ onto the PSS film was evident by the emergence of a sharp absorption band of the $AuCl_4^-$-CTA^+ complex at 320 nm (cf. Figure S1, Supporting Information, SI).[42,43] Upon UV irradiation, this characteristic band decreased and diminished quickly within 5 min, implying efficient reduction of gold precursors (Figure S2a, SI). Presumably, the embedded photocatalytic POM facilitates reduction of Au^{3+} in $AuCl_4^-$ via oxidation of isopropanol. Subsequently, the broad absorption around 530 nm gradually became more easily identifiable but then saturated within 3 hr (cf. inset of Figure 2), signifying slow aggregation of gold atoms into NPs.[43]

2.2. Structure of Au-NP@ PSS

Figure 3a,b shows the TEM image taken for an Au-NP@PSS film, exhibiting highly oriented channels of densely populated Au NPs. (More TEM images in different length scales are shown in Figure S3, SI.) From the high resolution TEM image shown in Figure 3c, a mean size ca. 1.7 nm was estimated for the Au NPs. The statistic NP spacing along the silicate nanochannels is

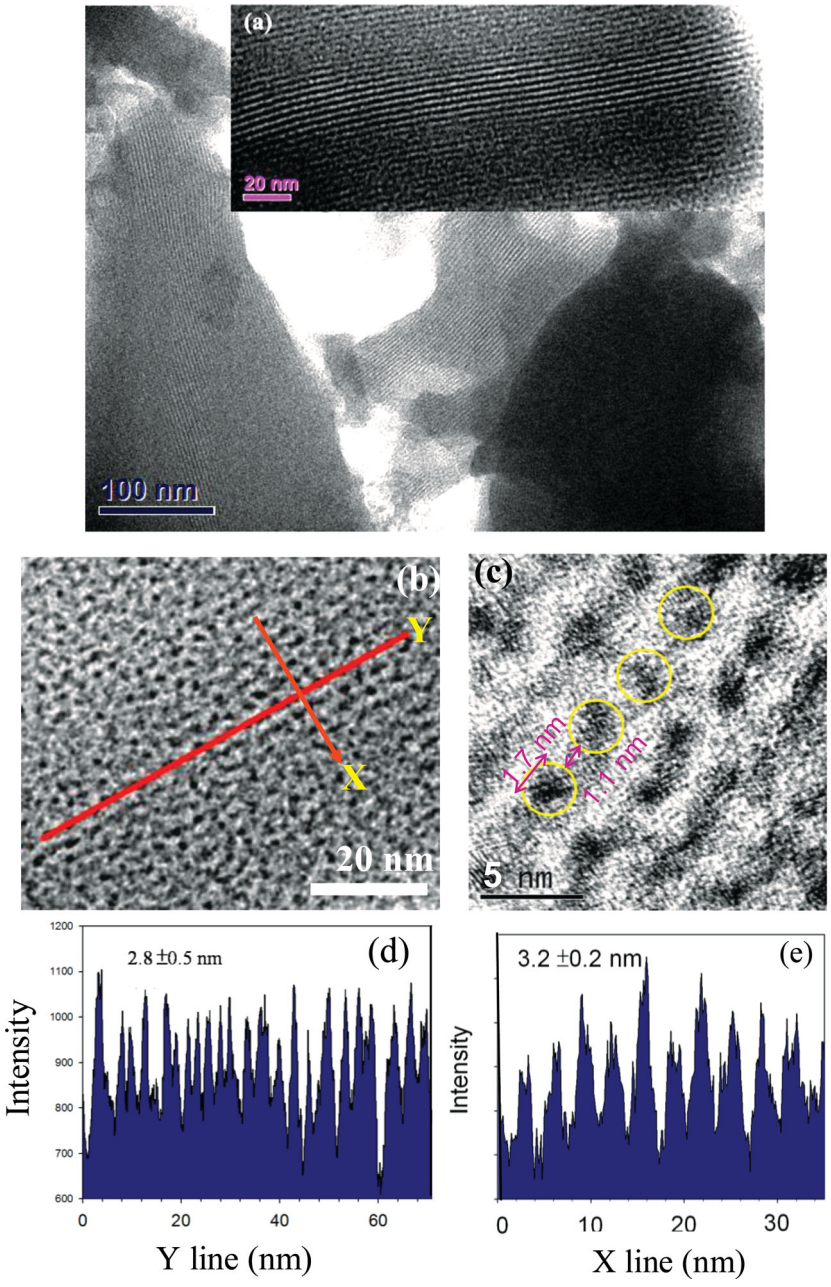

Figure 3. a) Representative TEM images of an Au-NP@PSS film, showing highly oriented nanochannels (dark stripes) of densely populated Au NPs, as further detailed in (b). c) A high-resolution TEM image illustrating the closely packed Au NPs of 1.7 nm size (dark spots representatively circled), aligned along the channels with a mean NP gap of 1.1 nm. d,e) Respectively, the Au-NP probability profiles extracted along (Y-line) and perpendicular (X-line) to the channels in (b), illustrating respectively a mean NP spacing of 2.8 nm (averaged peak-to-peak distance) along the channel and a mean inter-channel spacing of 3.2 nm.

2.8 nm (Figure 3d) whereas the mean inter-channel (center-to-center) spacing of the Au NP arrays is 3.2 nm (Figure 3e). After subtracting the NP size, the deduced NP gaps are 1.1 nm along the NP arrays and 1.5 nm between adjacent arrays.

X-ray energy-dispersive spectroscopic (EDS) result (Figure S4, SI) exhibits Au signals throughout the Au-NP@PSS film. Thermogravimetric analysis (TGA) (Figure S5, SI) reveals consistently a high level (73 wt%) of Au NPs in the Au-NP@PSS film. Nevertheless, TGA for an $AuCl_4^-$@PSS film fully saturated with $AuCl_4^-$ adsorption (before UV irradiation) indicates only 44 wt% of Au within the film. Apparently, multiple-adsorption of free $AuCl_4^-$ (after reduction of the first adsorption batch) is needed to provide sufficient gold atoms in saturating the silicate-surfactant channels of the PSS film with 73 wt% Au NPs. The multiple-adsorption process was indeed evidenced from the decay-and-growth cycles of the 320 nm band of the UV-vis spectra (Figure S2b, SI). Also revealed from TGA is the non-trivial (8 wt%) presence of PTA (Figure S5, SI). From the weight ratio of PTA to Au NP and the Au NP size (1.7 nm), we further deduce a substantially high number ratio 1:1 of PTA to Au NP in the Au-NP@PSS film.

Prolonged UV irradiation to 24 h for the Au-NP@PSS film led to a marginal increase in size and number density of the NPs, as revealed from TEM images. Nevertheless, packing of Au atoms inside the NP particles was substantially improved (Figure S3b, SI). This is consistent with broad humps (due to limited size) of the face-centered-cubic structure of Au NPs[17,22] in the X-ray diffraction (XRD) profile (**Figure 4**a) of the Au-NP@PSS composite. From the XRD peak widths, a crystalline domain size of 1.7 nm for the Au NPs could be estimated using the Scherrer equation. The mean NP size determined via transmission small-angle X-ray scattering (SAXS) is 1.7 (±0.2) nm with 5% polydispersity (Figure S6, SI), in excellent agreement with TEM and XRD results.

Shown in Figure 4b are in-situ grazing-incidence SAXS (GISAXS) profiles of a PSS template film at the air-water interface before and after formation/incorporation of Au NPs (Figure S7, SI). The prominent GISAXS reflections indicate an ordered POM-silicatropic mesophase from self-assembled POM-silica-surfactant micelles at the air-water interface. The relative peak positions of $1 : 3^{1/2} : 2$ suggest 2D hexagonal (H) packing with lattice parameter $a = 4.24$ nm (as deduced from the first peak position at $q = 1.482$ nm^{-1}).[37] The ordered domain size estimated from the peak width is ca. 0.5 μm.[37] During adsorption and reduction of Au precursors for the Au-NP@PSS composite, the GISAXS peak positions remained largely unaltered (Figure 4b). However, gradually enhanced peak intensities at the same peak positions (attributable to enhanced scattering contrast upon Au NP formation) indicate that formation and distribution of Au NPs were well-directed by the photocatalytic channels of the PSS template. All results from UV-vis adsorption, TGA, TEM,

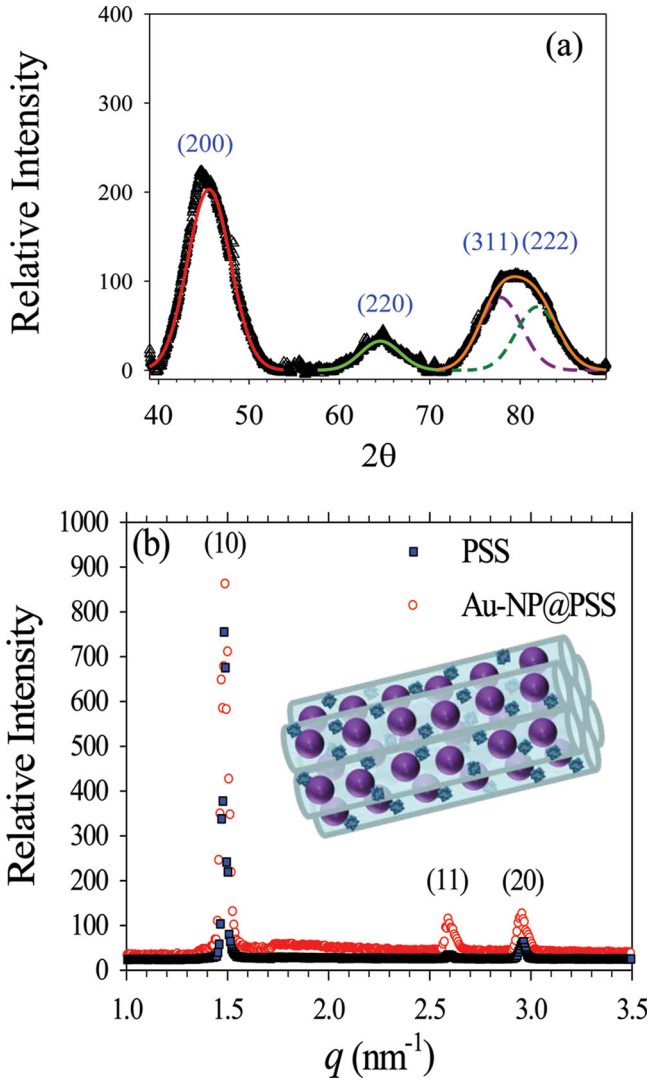

Figure 4. a) Broad peaks of the XRD profile for the Au-NP@PSS composite are fitted (solid curves) and indexed according to the characteristic FCC reflections of Au crystallites. b) GISAXS profiles of the PSS template and the subsequently formed Au-NP@PSS film at the air-water interface. These two sets of GISAXS profiles, of identical peak positions, are indexed with 2D hexagonal packing of a same lattice. The stronger GISAXS peaks for the Au-NP@PSS case are attributed to enhanced scattering contrast upon formation of Au NPs of a higher electron density. The cartoon in the inset illustrates the H domain comprising 2D hexagonally packed silica channels stuffed with Au NPs (purple spheres) and PTA (squares).

XRD, SAXS, and GISAXS measurements suggest consistently that nearly monodisperse and largely crystalline Au NPs were homogeneously formed and arrayed into the mesostructured Au-NP@PSS film, as illustrated in the cartoon in the inset of Figure 4b. Moreover, after harvested from the air-water interface, the composite film (centimeters in lateral dimensions and micrometers in film thickness) maintained its integrity with moisture. Upon drying, the films cracked into flakes of smaller sizes; nevertheless, H-domain structure in the smaller flakes was well-retained, as revealed by H-reflections in the GISAXS profile of a film transferred onto a Si wafer (cf. Figure S8e, SI).

We note that the silica inter-channel spacing deduced from the lattice constant of a fully hydrated Au-NP@PSS film at the air-water interface is 4.84 nm, which is significantly greater than that (3.2 nm) observed from the TEM image (cf. Figure 3) for the dried Au-NP@PSS film (without calcination). The shrinkage by 1.6 nm in the mean channel spacing for the TEM sample may be attributed to the collapse of the lyotropic phase (due to depletion of water in the channels) upon film drying. This observation suggests available channel space of the Au-NP@PSS composite to accommodate small guest molecules in solution, as evidenced by SERS results below.

2.3. SERS of Au-NP@PSS

To demonstrate SERS effects of the densely packed Au NPs (ca. 2 nm in diameter) with small gaps (1–2 nm) in the Au-NP@PSS composite, we have conducted SERS measurements with the composite after soaking in a solution of 1 mM 4-MBA. Shown in **Figure 5** is the prominent SERS spectrum of 4-MBA, exhibiting two especially sharp bands at 1077 and 1600 cm^{-1}. In contrast, a much dimmer SERS spectrum (inset of Figure 5) was observed with randomly distributed 2-nm Au NPs (of the same total Au content/NP surface area) after soaking in a similar 4-MBA solution. This clearly illustrates the NP packing effect on SERS. Specifically, with mean NP gaps of 1–2 nm along and across the NP arrays, the Au-NP@PSS composite has an ultrahigh number density of hot spots from the 3D nanometer-spaced Au NPs amounting to $\approx 10^{19}$ NP cm^{-3} (deduced based on the structural parameters obtained from the X-ray and TEM results). Advantages of 2D hexagonally arrayed metallic NPs for hot-spot EM field enhancements within the arrays were previously shown via calculations[2,3] but this is the first experimental demonstration with NPs of such limited size of ≈2 nm.

The strong electron acceptor PTA (embedded in the silica channels of the PSS template for photocatalytic reduction of Au precursors) may have a second role of promoting SERS performance after NP formation.[44,45] Respective SERS measurements on Au NPs with and without PTA-attachment showed enhancement of SERS response for 4-MBA by a factor of 5 to 10 (cf. Figure S9, SI). PTA-facilitated charge transfer between metallic NPs and surrounding matrix was employed in catalytic reactions with metallic NPs,[24,46,47] where the "chemical" enhancement in SERS was attributed to.

According to results of DFT calculations [29–32,48,49] for 4-MBA monomers anchored on Au atoms (Figure 5), the two most prominent 1077 and 1600 cm^{-1} bands are assigned respectively to the modified breathing and C–C stretching modes of phenyl ring upon attachment to an Au NP. The 1187 cm^{-1} band is assigned to coupled CH- and OH-bending (near the S atom of 4-MBA) and the broader 1294 cm^{-1} band to coupled C–C stretching of the ring, C–O stretching of the carboxylic group, and -OH bending. The weaker 991 cm^{-1} band may correspond to in-plane vibrations of the ring. Assignments of these bands (cf. movies of normal modes, SI) are consistent with previous reports.[30,50] The appearance of twin 800/810 cm^{-1} bands in Figure 5, however, reveals unusual symmetric and anti-symmetric modes of CC(S)C- and CC(O)-bending coupled through hydrogen bonding of the carboxylic groups of two

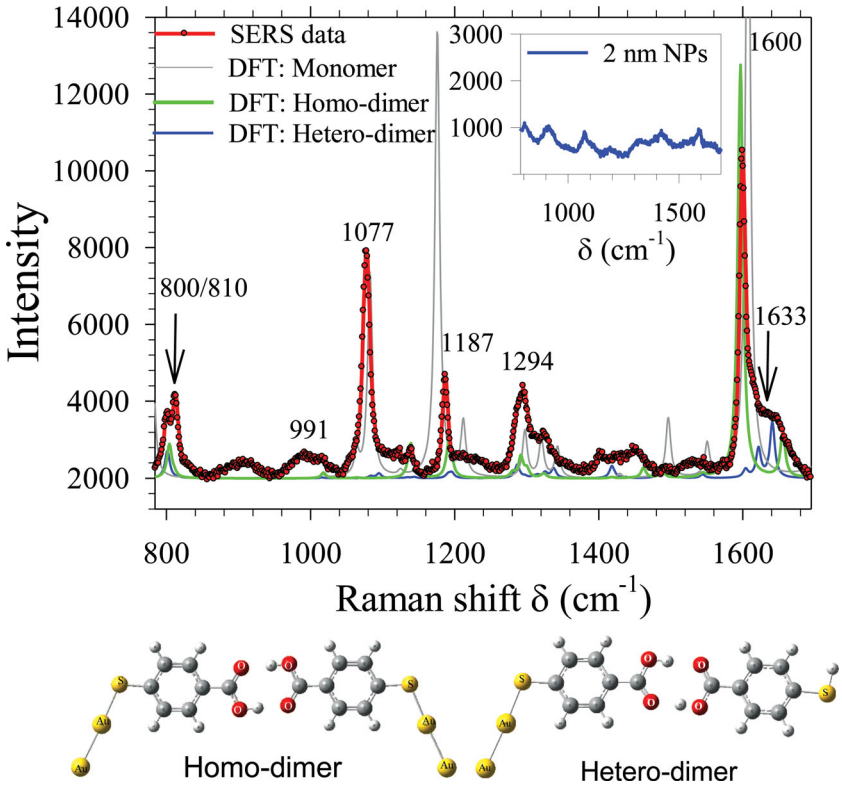

Figure 5. SERS spectra obtained with 532 nm laser excitation for 1.7-nm Au-NP@PSS composite and dispersed 2-nm Au NPs of a same total Au weight (inset), respectively soaking in solutions of 1 mM 4-MBA. Also shown are DFT-calculated spectra for monomer, hetero-dimer, and homo-dimer of 4-MBA, bound on Au NPs. The arrows mark the characteristic bands (near 800 and 1633 cm^{-1}) contributed mainly by the two types of 4-MBA dimers (cartoons at the bottom).

4-MBA in a dimer form. Similarly, the broader shoulder near 1600 cm^{-1} may correspond to the calculated 1633/1653 cm^{-1} bands (Figure 5) from coupling of CO stretching and OH bending of 4-MBA hetero-dimers with one 4-MBA bound to an Au NP) and homo-dimers with both 4-MBA anchored to Au NPs (cf. cartoons at the bottom of Figure 5). These characteristic SERS modes, successfully depicted via modeled Raman tensors in DFT calculations in terms of 4-MBA monomers and dimers attached to Au NPs, reveal that 4-MBA could enter into the PTA-silica channels of the Au-NP@PSS composite and form preferred S–Au bonding with Au NPs. As the silica channels of the Au-NP@PSS composite have limited channel space, the linearly coupled 4-MBA dimers suggested by the DFT calculations should orient along the channels as illustrated in **Figure 6**. With a long axis of ≈1 nm, 4-MBA molecules must be oriented along the channel direction to enter the channel space.

We have systematically measured SERS spectra with 633 nm laser excitation for the Au-NP@PSS composite after soaking in 1 mM, and 100, 10, and 1 μM 4-MBA solutions, respectively (Figure S10a, SI). The two characteristic bands of 4-MBA centered at 1074 and 1588 cm^{-1} could be clearly observed even in the case with 1 μM 4-MBA solution. In accord with previous SERS studies,[7,51] we have estimated the SERS enhancement factor EF of the Au-NP@PSS film for the SERS bands using

$$EF = (I_{Au} / C_{Au}) / (I_{ref} / C_{ref}) \quad (1)$$

where I_{Au} and I_{ref} are the corresponding band intensities of Au-NP@PSS and PSS films (of a same PSS weight) after soaking in 4-MBA solutions of concentrations C_{Au} and C_{ref}, respectively. Compared to the Raman spectrum for 4-MBA adsorbed to a PSS film without Au NPs, the SERS spectrum of the 4-MBA-Au-NP@PSS film soaked in 1-μM 4-MBA solution displays reasonably good *EF* values 8×10^4 and 4×10^4 respectively for the 1074 and 1588 cm^{-1} bands. Furthermore, these *EF* values tend to increase with decreasing 4-MBA concentration for soaking of the Au-NP@PSS composite (Figure S10b, SI), implying that the EF value may be limited by saturation of 4-MBA in the channels. In other words, not all 4-MBA molecules in the solution could enter the channel space; the EF value corresponds to an average over all 4-MBA molecules, with or without Au-NP adsorption.

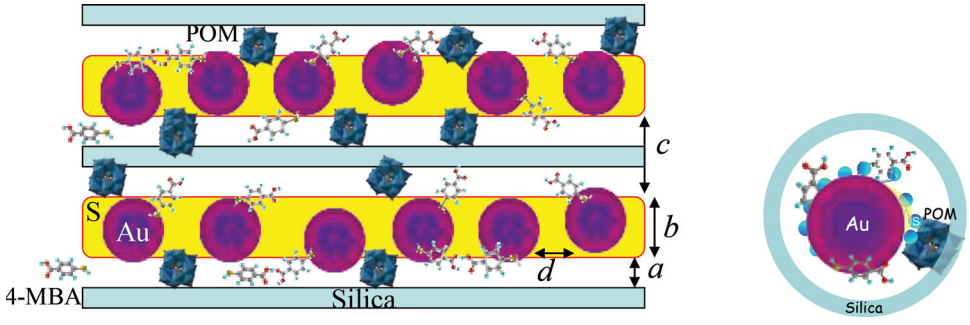

Figure 6. Cartoons for the side and top views of the 4-MBA-adsorded PTA-silica channels of Au-NP@PSS, illustrating SERS hot channels formed with densely packed arrays of nanometer-spaced Au NPs. The characteristic dimensions, *a*, *b*, *c*, and *d*, are respectively ca. 1, 2, 3, and 1–2 nm. Symbol S denotes the region (yellow zones) of surfactant micelles in the channel centers.

Average SERS *EF* values measured can be corrected with an assumed molecular adsorption efficiency toward NPs for the "extrapolated" EF value according to that shown in previous reports.[7,51] Instead, we chose to improve the molecular adsorption efficiency to the Au NPs by enlarging the silica channel space. This was achieved by replacing C_{16}TAB with C_{18}TAB for the synthesis of Au-NP@PSS-18, also of H-phase structure. The greater channel cross-section formed with C_{18}TAB provides an enlarged channel space (by ≈20%), an increased silica interchannel distance (by 0.6 nm), and a slightly larger Au NP size of 2.1 nm, as revealed by TEM and GISAXS (Figure S11, SI). As shown in **Figure 7**a, Au-NP@PSS-18 extends the sensitivity with 4-MBA in solution to 50 nM, compared to the 1 μM limit of Au-NP@PSS-16 (Figure S10a, SI). Correspondingly, the measurable *EF* values for the characteristic 1074 and 1588 cm^{-1} bands are significantly improved to 10^6 (cf. Figure S8c). To further increase the channel space, we depleted surfactants in the Au-NP@PSS-18 composite using ultraviolet radiation/ozone treatment. Note that the structure of arrayed Au NPs is largely preserved in the O_3-treated sample (cf. TEM images in Figure S12, SI). As shown in Figure 7b, the 4-MBA detection limit of the O_3-treated composite reached 5 nM; improvement of EF to 10^8 for the two characteristic SERS modes was obtained with the surfactant-depleted Au-NP@PSS-18 (cf. Figure 7c). We note that the in-plane vibration mode of the 4-MBA phenyl ring at 991 cm^{-1} is increasingly better enhanced (as compared to the characteristic modes at 1074 and 1588 cm^{-1} for the breathing and C–C stretching modes of the ring) when the 4-MBA concentration is below 1 μM (cf. Figure 7b), implying changes of 4-MBA morphological features (tethered vs bridging) in the composite channels on the basis of the assigned molecular adsorption configurations.

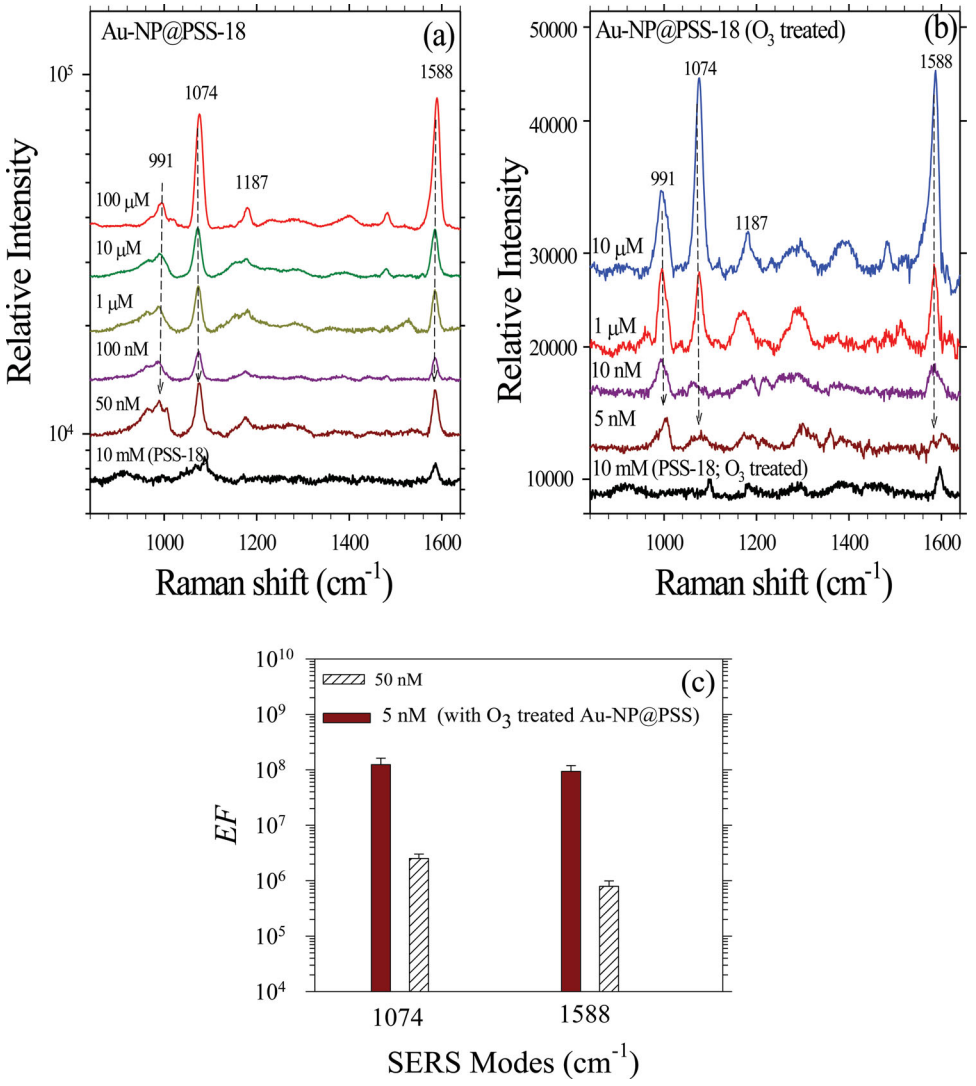

Figure 7. a) SERS spectra with 633-nm laser excitation for the Au-NP@PSS-18 composite, 18 h after soaking in 4-MBA solutions of the concentrations indicated. Also shown is the spectrum for a neat PSS-18 film (without Au-NP loading) after soaking in a solution of 10 mM 4-MBA. b) SERS spectra measured for the surfactant-depleted Au-NP@PSS-18 and PSS-18, after soaking respectively in solutions with the 4-MBA concentrations indicated. c) Best enhancement factor (EF) for the representative SERS modes deduced respectively from (a,b), as indicated.

The SERS results indicate that the new material Au-NP@PSS composite with densely spaced Au NPs can exhibit impressive SERS, which is likely attributable to the high number density of SERS hot spots for near-filed LSPR.[27] The PTA-embedded channels further provides an environment for adjunctive chemical enhancement.[27,28] With the high SERS performance and the special channel environment, Au-NP@PSS composite may find applications in molecular sensing with sieving, with size-exclusion characteristics. [1,52,53] For instances, a trace amount of targeted small molecules (of a similar 4-MBA size ≈1 nm) in a solution mixture, can enter into the PTA-silica channels of the Au-NP@PSS composite and be sensed and identified via selected SERS, without interferences from large molecules in the mixture.

3. Conclusions

We have developed a synthesis scheme via an air-water interface, allowing homogeneous and continuous reduction of metallic ions inside photocatalytic silica channels for sustained filling of NPs until saturation. The hence fabricated new material of Au-NP@PSS has 2D hexagonal arrays of densely spaced (1–2 nm) Au NPs of ≈2 nm. Beyond a general low SERS expectation with small metallic NPs, the Au-NP@PSS composite can exhibit impressive SERS performance attributable to the rich SERS hot spots from the very high number density of Au NPs (≈10^{19} NPs cm^{-3}), together with an adjunctive chemical enhancement from the PTA-embedded channel environment. The corresponding 4-MBA detecting concentration limit is down to 5 nM, with a prominent SERS EF ≈10^8. With the brilliant SERS performance and the special PTA-channel environment, the Au-NP@PSS composite may have potential applications in molecular sensing with sieving. With the ultra-high number density of Au NPs surrounded by abundant PTA in the vicinity for efficient charge transfer, the Au-NP@PSS composite may also be useful in other applications, including channel-confined catalytic reactions. Easy synthesis and large film dimensions are additional advantages of the new material in practical applications. Moreover, the proposed synthesis based on the POM-silicatropic template at the air-water interface may be extended for similar noble metallic-NP@PSS films (Pt or Ru) for diversified applications.

4. Experimental Section

Synthesis of PSS Template and Au-NP@PSS Films: Polyoxometalate-silica-surfactant films were self-assembled at the air-water interface from an acidic (pH < 2) solution comprising H_2O : HCl : cetyltrimethylammoium bromide (C_{16}TAB) : tetraethyl orthosilicate (TEOS) : $PW_{12}O_{40}^{3-}$ (PTA^{3-}) = 100 : 2.0 : 0.11 : 0.36 : 0.00015 in molar ratio, which corresponded to 80 μM in PTA^{3-} concentration. The composition was used to form free-floating films of thermodynamically favored silicatropic phase of 2D hexagonal (H) packing, as shown in previous reports.[37,54] Addition of PTA up to 1 mM did not alter the preferred H phase of the films; the films processed with higher PTA concentrations approaching 1 mM, however, became relatively brittle upon film drying. The sample solution trough for film formation was sealed in an air-tight box for a saturated solution vapor pressure at 298 K. Formation of a self-assembled PSS film free-floating at the air-water interface could be observed after several minutes of induction time; the film then gradually thickened and matured within 3 h. Subsequently, a small amount of $HAuCl_4$ solution in isopropanol/water was injected into the solution subphase under the free floating PSS film. Uniform adsorption of $HAuCl_4$ to the pale PSS film was evident from uniform film color transition to orange-yellow within 30 min. The $HAuCl_4$ adsorbed PSS film at the air-water was then subject to UV irradiation for a few hours (with a xenon arc lamp) for the final product of Au-NP@PSS film of a thickness ranging from a few to hundreds micrometers and lateral dimensions from tens to hundreds millimeters, depending on the trough size and reaction time (Figure S13, SI). The adsorption and reduction of Au precursors and the formation of Au NPs were monitored with UV-vis absorption using a J&M TIDAS S diode array spectrophotometer.

Grazing-Incidence Small-Angle X-Ray Scattering (GISAXS): Formations of the PSS and subsequent Au-NP@PSS films at the air-water interface were observed in situ using the GISAXS setup of the 23A SWAXS endstation at the National Synchrotron Radiation Research Center (NSRRC), Hsinchu.[55] A similar sample solution as described previously for film formation was filled into a Teflon trough, giving 80 mm × 80 mm in air-water interface area and 0.7 mm in depth. The trough was then enclosed in an air-tight Al box (for saturated water vapor pressure) with Kapton windows for X-ray incidence. With a 10 keV beam (0.15 mm in size) and an incident angle of 0.15°, GISAXS patterns from the air-water interface were collected at 298 K using a MAR165CCD area detector. Following the sample preparation procedure detailed previously, GISAXS patterns were collected for the subsequent adsorption of $HAuCl_4$ to the PSS film and the formation of Au-NP@PSS film during UV irradiation. The scattering wavevector q ($= 4\pi\lambda^{-1}\sin\theta$) defined by the scattering angle 2θ and X-ray wavelength λ was calibrated using the scattering from silver behenate.[55]

SERS Measurements: SERS samples were prepared by submerging Au-NP@PSS composites in methanol solutions containing different concentrations (1 mM to 5 nM) of 4-MBA for 18 h. After centrifugation, the samples were dispensed on Al substrates for SERS measurements. SERS spectra were collected using an in-house system (cf. SI) or a Uni-Ram system equipped with a TE-cooled CCD (1024 × 128 pixels) and a 532-nm or 633-nm diode laser (Protrustech), with a laser spot size 1.2 mm and a beam power density of 20 mW cm^{-2}. The laser exposure time was 10 s for each spectrum. Data were averaged from 10 to 100 spectra (depending on sample scattering intensity) for improved statistics.

Density Functional Theory (DFT) Simulation: All DFT calculations were performed using Gaussian09 package[29,30] with I/O format being locally modified. All system geometries were optimized and the Raman frequencies for the optimized structures were computed. The DFT calculations were carried out at B3LYP[31] level with 6-311++G(p,d) basis sets[32] for hydrogen, carbon, oxygen and sulfur and SDD basis sets[48] and the corresponding effective core potential for gold. Raman intensities were simulated using coupled-perturbed Kohn-Sham theory[49] under several assumptions, including pre-resonance conditions.[56–58]

Supporting Information

Supporting Information is available from the Wiley Online Library or from the author.

Acknowledgements

The authors thank K.-F. Liao, C.-H. Su and Y.-J. Chen for the assistance with GISAXS measurements, and Dr. B.-J. Hwang for the use of Raman spectrometer. Financial supports from the National Science Council (grant numbers NSC-98-2113-M-029-006-MY2 and NSC 102-2112-M-213-005-MY3) are gratefully acknowledged.

Received: November 2, 2013
Revised: November 12, 2013
Published online: January 6, 2014

[1] a) L. Guerrini, E. Pazos, C. Penas, M. E. Vázquez, J. L. Mascareñas, R. A. Alvarez-Puebla, *J. Am. Chem. Soc.* **2013**, *135*, 10314–10317; b) V. López-Puente, S. Abalde-Cela, P. C. Angelomé, R. A. Alvarez-Puebla, L. M. Liz-Marzán, *J. Phys. Chem. Lett.* **2013**, *4*, 2715–2720.
[2] a) J. T. Theiss, P. Pavaskar, P. M. Echternach, R. E. Muller, S. B. Cronin, *Nano Lett.* **2010**, *10*, 2749–2754; b) A. Chen, A. E. DePrince, A. Demortière, A. Joshi-Imre, E. V. Shevchenko, S. K. Gray, U. Welp, V. K. Vlasko-Vlasov, *Small* **2011**, *7*, 2365–2371.
[3] a) P. K. Jain, M. A. El-Sayed, *Nano Lett.* **2008**, *12*, 4347–4352; b) D. A. Genov, A. K. Sarychev, V. M. Shalaev, A. Wei, *Nano Lett.* **2004**, *4*, 153–158; c) R. Thomas, R. S. Swathi, *J. Phys. Chem. C* **2012**, *116*, 21982–21991; d) J. Bochterle, F. Neubrech, T. Nagao, A. Pucci, *ACS Nano* **2012**, *6*, 10917–10923.
[4] H. H. Wang, C. Y. Liu, S. B. Wu, N. W. Liu, C. Y. Peng, T. H. Chan, C. F. Hsu, J. K. Wang, Y. L. Wang, *Adv. Mater.* **2006**, *18*, 491–495.
[5] B. Yan, A. Thubagere, W. R. Premasiri, L. D. Ziegler, L. D. Nergo, B. M. Reinhard, *ACS Nano* **2009**, *3*, 1190–1202.
[6] C. Forestiere, A. J. Pasquale, A. Capretti, G. Miano, A. Tamburrino, S. Y. Lee, B. M. Reinhard, L. D. Negro, *Nano Lett.* **2012**, *12*, 2037–2044.
[7] S. M. Adams, S. Campione, J. D. Caldwell, F. J. Bezares, J. C. Culbertson, F. Capolino, R. Ragan, *Small* **2012**, *14*, 2239–2249.
[8] R. Thomas, R. S. Swathi, *J. Phys. Chem. Lett.* **2012**, *116*, 21982–21991.
[9] K. L. Wustholtz, A. I. Henry, J. M. McMahon, R. G. Freeman, N. Valley, M. E. Piotti, M. J. Natan, G. C. Schatz, R. P. Van Dyune, *J. Am. Chem. Soc.* **2010**, *132*, 10903–10910.
[10] W. J. Cho, Y. Kim, J.K. Kim, *ACS Nano* **2012**, *6*, 249–255.
[11] E. C. Le Ru, E. Blackie, M. Meyer, P. G. Etchegoin, *J. Phys. Chem. C* **2007**, *111*, 13794–13803.
[12] L. F. Gutiérrez, S. Hamoudi, K. Belkacemi, *Catalysts* **2011**, *1*, 97–154.
[13] L. Bois, F. Chassagneux, C. Desroches, Y. Battie, N. Destouches, N. Gilon, S. Parola, O. Stéphan, *Langmuir* **2010**, *26*, 8729–8736.
[14] F. Chassagneux, L. Bois, J. P. Simon, C. Desroches, A. Brioudea, *J. Mater. Chem.* **2011**, *21*, 11947–11955.
[15] A. Virga, P. Rivolo, E. Descrovi, A. Chiolerio, F. Frascella, F. Giorgisb, *J. Raman Spectrosc.* **2012**, *43*, 730–736.
[16] C. M. Yang, H. A. Lin, B. Zibrowius, B. Spliethoff, F. Schuth, S. C. Liou, M. W. Chu, C. H. Chen, *Chem. Mater.* **2007**, *19*, 3205–3211.
[17] Y. J. Han, J. M. Kim, G. D. Stucky, *Chem. Mater.* **2000**, *12*, 2068–2069.
[18] C. Chen, C. Nan, D. Wang, Q. Su, H. Duan, X. Liu, L. Zhang, D. Chu, W. Song, Q. Peng, Y. Li, *Angew. Chem. Int. Ed.* **2011**, *50*, 3725–3729.
[19] H. Y. Lin, C. Y. Chin, H. L. Huang, W. Y. Huang, M. J. Sie, L. H. Huang, Y. H. Lee, C. H. Lin, K. H. Li, X. Bu, S. L. Wang, *Science* **2013**, *339*, 811–813.
[20] Y. Kanno, T. Suzuki, Y. Yamauchi, K. Kuroda, *J. Phys. Chem. C* **2012**, *116*, 24672–24680.
[21] R. Silva, A. V. Biradar, L. Fabris, T. Asefa, *J. Phys. Chem. C* **2011**, *115*, 22810.
[22] C. K. Tsung, W. B. Hong, Q. H. Shi, X. S. Kou, M. H. Yeung, J. F. Wang, G. D. Stucky, *Adv. Funct. Mater.* **2006**, *16*, 2225–2230.
[23] J. M. Sun, D. Ma, H. Zhang, X. Liu, X. Han, X. Bao, G. Weinberg, N. Pfander, D. Su, *J. Am. Chem. Soc.* **2006**, *128*, 15756–15764.
[24] W. Qi, H. Li, L. Wu, *J. Phys. Chem. B*, **2008**, *112*, 8257–8263.
[25] D. A. Doshi, A. Gibaud, V. Goletto, M. Lu, H. Gerung, B. Ocko, S. M. Han, C. J. Brinker, *J. Am. Chem. Soc.* **2003**, *125*, 11646–11655.
[26] D. Grosso, F. Cagnol, G. J. de A. A. Soler-Illia, E. L. Crepaldi, H. Amenitsch, A. Brunet-Bruneau, A. Bourgeois, Sanchez, C. *Adv. Funct. Mater.* **2004**, *14*, 309–322.
[27] S. L. Kleinman, B. Sharma, M. G. Blaber, A.-I. Henry, N. Valley, R. G. Freeman, M. J. Natan, G. C. Schatz, R. P. Van Duyne, *J. Am. Chem. Soc.* **2013**, *135*, 301–308.
[28] L. Tong, T. Zhu, Z. Liu, *Chem. Soc. Rev.*, **2011**, *40*, 1296–1304.
[29] M. Frisch, G. Trucks, H. Schlegel, G. Scuseria, M. Robb, J. Cheeseman, G. Scalmani, V. Barone, B. Mennucci, G. Petersson, *Wallingford CT* **2009**, *1*, 3.
[30] W.-Q. Ma, Y. Fang, G. Hao, W. Wang, *Chine. J. Chem. Phys.* **2010**, *23*, 659–663.
[31] M. J. Frisch, J. A. Pople, J. S. Binkley, *J. Chem. Phys.* **1984**, *80*, 3265–3269.
[32] A. D. Becke, *J. Chem. Phys.* **1993**, *98*, 5648–5652.
[33] H. P. Lin, C. Y. Mou, *Acc. Chem. Res.* **2002**, *35*, 927.
[34] G. J. d. A. A. Soler-Illia, C. Sanchez, B. Lebeau, J. Patarin, *Chem. Rev.* **2002**, *102*, 4093-4138.
[35] C. Yen, M. L. Lin, A. Wang, S. A. Chen, J. M. Chen, C. Y. Mou, *J. Phys. Chem. C* **2009**, *113*, 17831–17839.
[36] Q. Huo, D. I. Margolese, U. Ciesla, D. G. Demuth, P. Feng, T. E. Gier, P. Sieger, A. Firouzi, B. F. Chmelka, F. Schuth, G. D. Stucky, *Chem. Mater.* **1994**, *6*, 1176–1191.
[37] Y. H. Lai, S. W. Cheng, S. W. Chen, J. W. Chang, C. J. Su, A. C. Su, H. S. Sheu, C. Y. Mou, U. Jeng, *RSC Adv.* **2013**, *3*, 3270–3283.
[38] H. Yang, N. Coombs, I. Sokolov, G. A. Ozin, *Nature* **1996**, *381*, 589–592.
[39] a) K. J. Edler, *Soft Matter* **2006**, *2*, 284–292; b) T. Brenann, S. J. Roser, S. Mann, K. J Edler. *Chem. Mater.* **2002**, *14*, 4292–4299.
[40] S. A. Holt, J. L. Ruggles, J. W. White, R. F. Garrett, *J. Phys. Chem. B* **2002**, *106*, 2330–2336.
[41] M. C. Liu, H. S. Sheu, S. Cheng, *J. Am. Chem. Soc.* **2009**, *131*, 3998–4005.
[42] a) A. K. Gangopadhayay, A. Chakravorty, *J. Chem. Phys.* **1961**, *35*, 2206; b) K. Torigoe, K. Esumi, *Langmuir* **1992**, *8*, 59–63.
[43] V. Amendola, M. Meneghetti, *J. Phys. Chem. C* **2009**, *113*, 4277–4285.
[44] A. Troupis, A. Hiskia, E. Papaconstantinou, *Angew. Chem. Int. Ed.* **2002**, *41*,1911–1914.
[45] S. Mandal, P. R. Selvakannan, R. Pasricha, M. Sastry, *J. Am. Chem. Soc.*, **2003**, *125*, 8440–8441
[46] G. Maayan, R. Popovitz-Biro, R. Neumann, *J. Am. Chem. Soc.* **2006**, *128*, 4968–4969.
[47] W. B. Kim, T. Voitl, G. J. Rodriguez-Rivera, J. A. Dumesic, *Science* **2004**, *305*, 1280–1283.
[48] P. Schwerdtfeger, M. Dolg, W. H. E. Schwarz, G. A. Bowmaker, P. D. W. Boyd, *J. Chem. Phys.* **1989**, *91*,1762–1774.
[49] a) H. Sekino, R. J. Bartlett, *J. Chem. Phys.* **1986**, *85*, 976–989; b) J. E. Rice, N. C. Handy, *J. Chem. Phys.* **1991**, *94*, 4959–4971.
[50] T. Chen, H. Wang, G. Chen, Y. Wang, Y. Feng, W. S. Teo, T. Wu, H. Chen, *ACS Nano* **2010**, *4*, 3087–3094.
[51] F. L. Yap, P. Thoniyot, S. Krishnan, S. Krishnamoorthy, *ACS Nano* **2012**, *6*, 2056–2070.
[52] T. Konishi, M. Kiguchi, M. Takase, F. Nagasawa, H. Nabika, K. Ikeda, K. Uosaki, K. Ueno, H. Misawa, K. Murakoshi, *J. Am. Chem. Soc.* **2013**, *135*, 1009–1014.
[53] W. Li, R. Zamani, P. R. Gil, B. Pelaz, M. Ibáñez, D. Cadavid, A. Shavel, R. A. Alvarez-Puebla, W. J. Parak, J. Arbiol, A. Cabot, *J. Am. Chem. Soc.* **2013**, *135*, 7098–7101.
[54] M. Matheron, T. Gacoin, J.-P. Boilot, *Soft Matter* **2007**, *3*, 223–229.
[55] U. Jeng, C.-H. Su, C.-J. Su, K.-F. Liao, W.-T. Chuang, Y.-H. Lai, J.-W. Chang, Y.-J. Chen, Y.-S. Huang, M.-T. Lee, K.-L. Yu, J.-M. Lin, D.-G. Liu, C.-F. Chang, C.-Y. Liu, C.-H. Chang, K. S. Liang, *J. Appl. Cryst.* **2010**, *43*, 110–121.
[56] M. Noda, T. Yasuike, K. Nobusada, M. Hayashi, *Chem. Phys. Lett.* **2012**, *550*, 52–57.
[57] T. Yasuike, K. Nobusada, M. Hayashi, *Phys. Rev. A* **2011**, *83*, 013201.
[58] T. Yasuike, K. Nobusada, *Phys. Chem. Chem. Phys.* **2013**, *15*, 5424–5429.